Nano Research 2017, 10(9): 3035–3048
DOI 10.1007/s12274-017-1519-1
Research Article
ISSN 1998-0124
CN 11-5974/O4

Co-Co_3O_4@carbon core–shells derived from metal–organic framework nanocrystals as efficient hydrogen evolution catalysts

Yanyan Liu[1], Guosheng Han[1], Xiaoyu Zhang[1], Congcong Xing[1], Chenxia Du[1] (✉), Huaqiang Cao[2], and Baojun Li[1] (✉)

[1] *College of Chemistry and Molecular Engineering, Zhengzhou University, Zhengzhou 450001, China*
[2] *Department of Chemistry, Tsinghua University, Beijing 100084, China*

Received: 30 November 2016
Revised: 20 January 2017
Accepted: 6 February 2017

KEYWORDS
Co-metal–organic frameworks (MOFs),
core–shell,
$NaBH_4$ hydrolysis,
pyrolysis,
synergistic effect

ABSTRACT

Controllable pyrolysis of metal–organic frameworks (MOFs) in confined spaces is a promising strategy for the design and development of advanced functional materials. In this study, Co-Co_3O_4@carbon composites were synthesized via pyrolysis of a Co-MOFs@glucose polymer (Co-MOFs@GP) followed by partial oxidation of Co nanoparticles (NPs). The pyrolysis of Co-MOFs@GP generated a core–shell structure composed of carbon shells and Co NPs. The controlled partial oxidation of Co NPs formed Co-Co_3O_4 heterojunctions confined in carbon shells. Compared with Co-MOFs@GP and Co@carbon-*n* (Co@C-*n*), Co-Co_3O_4@carbon-*n* (Co-Co_3O_4@C-*n*) exhibited higher catalytic activity during $NaBH_4$ hydrolysis. Co-Co_3O_4@C-II provided a maximum specific H_2 generation rate of 5,360 $mL \cdot min^{-1} \cdot g_{Co}^{-1}$ at room temperature due to synergistic interactions between Co and Co_3O_4 NPs. The Co NPs also endowed Co-Co_3O_4@C-*n* with the ferromagnetism needed to complete the magnetic momentum transfer process. This assembly-pyrolysis-oxidation strategy may be an efficient method of preparing novel nanocomposites.

1 Introduction

Metal–organic frameworks (MOFs) have emerged as a family of novel functional materials and attracted significant attention because of their highly ordered structures, tunable porosities, high surface areas, and special coordinated metal atoms [1–4]. These unique structural features lead to new potential applications for MOFs as pyrolysis precursors for use in synthesizing highly complex composite functional materials. Using MOFs, some types of organic and inorganic-carbon (C) composites including carbon nanostructures (carbon matrices, carbon sheets, carbon shells, etc.), metals@C, metal oxides@C, and metal oxide composites have been fabricated via various pyrolysis processes [5–8]. Research on controlling the morphologies of carbon

Address correspondence to Chenxia Du, dcx@zzu.edu.cn; Baojun Li, lbjfcl@zzu.edu.cn

and inorganic components continues. A confined space may be an ideal setting for controllable pyrolysis of MOFs. Novel products with interesting structures and properties are sometimes produced when synthesis occurs in confined spaces [9–12]. There are many reactions for which single-component inorganic nanoparticles (NPs) cannot provide satisfactory catalytic performance. The formation of second components on some metal NPs as surface clusters or shells in order to form heterojunctions may generate unexpectedly high catalytic performance due to the corresponding electronic interactions between various components. The well-designed, hierarchical, hollow ball-in-ball structure of NiO/Ni/graphene composites exhibited superior performance as an anode material in lithium ion batteries [13]. Thin-film catalysts (Sn^0-SnO_x) were also prepared in an attempt to enhance CO_2 reduction activity [14]. Coupling of Pd with pyridinic-nitrogen-doped carbon boosts catalytic activity for the dehydrogenation of formic acid [15]. Co@Co_3O_4@carbon-carbon matrix (C–CM) produced via ZIF-9 pyrolysis produced promising catalytic activity and stability to oxygen reduction [16]. The intrinsic activities of Co-based catalysts were improved via partial oxidation, resulting in efficient CO_2 electroreduction [17]. $Co^{II}Fe^{III}Co^{III}O_4$ spinel with Fe and Co co-occupying an inverse structure exhibited promising oxygen reduction reaction (ORR) activity [18]. These recent significant advances demonstrate the efficiencies of core–shell heterojunctions and other composites.

Because of its safety and renewability, hydrogen may serve as an excellent carbon-neutral medium for storage of energy generated from wind and solar-powered sources. Stable, efficient hydrogen production has been a focus of significant research, and some progress has been achieved [19–23]. The hydrolysis of sodium borohydride ($NaBH_4$) and ammonia borane ($NH_3{\cdot}BH_3$) can be used to produce high-purity hydrogen because the associated processes completely avoid the production of toxic CO. For safety, $NaBH_4$ can be reliably stabilized in an alkaline solution. Catalysts play an important role in controlling the speed and extent of hydrogen generation [24–26]. Because of the high cost and limited supply of noble metal catalysts (Pt, Rh, Ru), and low activities of Ni and Fe catalysts, cobalt-based catalysts are considered excellent options due to their low cost, nontoxicity, and high activities [24, 27–30]. Cobalt-based catalysts such as Co salts, $LiCoO_2$, CoO_x, Co^0 nanoparticles, Co-based alloys, Co borides, and supported Co catalysts exhibit moderate activity and poor stability. Nanoscale control of the shapes and structures of catalytically active particles can boost the catalytic activity significantly. Recently reported CoO nanorods and Co@C_2N catalysts exhibit outstanding catalytic activities (close to those of precious metal catalysts) but relatively poor catalytic stability [29, 30]. However, the poor stability of single-component cobalt-based catalysts in liquid reaction systems is the most significant barrier to wide adoption of these materials. The stability of these catalysts in liquid reactions may be improved by coating them with carbon or other atomic layers to form core–shell structures. Carbon and other atomic layers can prevent Co NPs from leaching, aggregating, and growing. The main challenge is to develop heterogeneous, cobalt-based catalysts with composite structures via novel preparation routes. These new catalyst structures and preparation methods are also suitable for other approaches to hydrogen production, such as electrolysis of H_2O and decomposition of formic acid. In a confined space, pyrolysis of MOFs produces appropriate multilayer composite structures. If the confined space relies on a carbon shell, a hierarchical composite is produced after thermal treatment. When CoO_x is used as the precursor, the catalytic active phase provides higher catalytic activity than metallic Co [29, 30]. To enable higher catalytic performance, Co-CoO_x heterojunctions should be constructed via partial oxidation of Co NPs. The presence of Co NPs can endow composite catalysts with super-paramagnetism and ensure complete, efficient magnetic momentum transfer by acting as nanoactuators [31–33]. Combining the above strategies can provide an ideal solution to a challenging problem.

In this study, ZIF-67 (Co-MOF) nanocrystals were synthesized and wrapped in glucose polymer shells to form Co-MOF@glucose polymer (Co-MOF@GP). Co-MOF@GP was pyrolyzed to generate a core–shell structure composed of carbon shells and Co NP cores. The controlled partial oxidation of Co NPs formed Co-CoO_x heterojunctions encapsulated in carbon shells. When using these composite materials as catalysts,

different catalytic activities toward $NaBH_4$ hydrolysis reaction were obtained via magnetic momentum transfer. Co-Co_3O_4@carbon-*n* (Co-Co_3O_4@C-*n*) exhibited higher catalytic activity than Co-MOF@GP or Co@carbon-*n* (Co@C-*n*). Co-Co_3O_4@C-II exhibited of a maximum specific H_2 generation rate of 5,360 $mL \cdot min^{-1} \cdot g_{Co}^{-1}$ at room temperature. The controllable pyrolysis of MOFs and construction of heterojunctions in confined spaces may have broad applications for the design and development of advanced functional materials.

2 Experimental section

2.1 Chemicals

Cobalt nitrate hexahydrate ($Co(NO_3)_2 \cdot 6H_2O$, Aladdin Industrial Co., Ltd., AR), 2-methylimidazole (MeIM, Energy Chemical Reagent Co., Ltd., AR), triethylamine ($C_6H_{15}N$, Sinopharm Chemical Reagent Co., Ltd., China, AR), anhydrous glucose ($C_6H_{12}O_6$, Tianjin Fengchuan Chemical Reagent Co., Ltd., AR), and distilled water were used as received. All of the chemicals are used without any further purification.

2.2 Material synthesis

Co-MOF nanocrystals were prepared by modifying a previously published method [34, 35]. The Co-MOF@GPs were produced as follows: Co $(NO_3)_2 \cdot 6H_2O$ (0.359 g) was dissolved in H_2O (25 mL). 2-methylimidazole (1.622 g) was dispersed in H_2O (25 mL), after which triethylamine (3 mL) was added and the mixture was sonicated for 10 min. After 5 min of stirring, the solution was rapidly mixed with the aforementioned cobalt nitrate solution and left to stir again for 18 h at room temperature. After 30 min of ultrasonication and agitation, the aqueous glucose solution (0.66 g glucose in 5 mL H_2O) was added drop wise into the above mixture and agitated for an additional 1 h. Next, the mixture was transferred into a Teflon-lined stainless steel autoclave (150 mL), heated to 140 ℃, and maintained there for 24 h. After cooling to room temperature, the resulting reddish violet powders were separated via centrifugation (5,000 rpm, 5 min), washed with water, and dried in air at 70 ℃ for 8 h. As-made powder samples were labeled Co-MOF@GP.

Co-MOF@GP was heated to 600 ℃ at a rate of 3 $℃ \cdot min^{-1}$ under flowing N_2 and annealed for 1 h. After being allowed to cool to room temperature naturally, the black powder was added to ethanol to form a new solution (35 mL) (Caution! The sample readily combusts when exposed to air). After magnetic separation and 10 h of drying at 35 ℃, the Co@C samples were retrieved and labeled Co@C-I. Following similar procedures, Co@C-II and Co@C-III were produced by annealing Co-MOF@GP at 700 and 800 ℃, respectively. Activating Co@C-I, Co@C-II, and Co@C-III in air at 200 ℃ for 22 h, produced Co-Co_3O_4@C-I, Co-Co_3O_4@C-II, and Co-Co_3O_4@C-III, respectively. Co@C-II was treated in air at different temperatures for various durations to provide control samples labelled Co-Co_3O_4@C. Porous Co_3O_4-I was obtained when Co@C-II was treated at 300 ℃ for 22 h. Porous Co_3O_4-II and Co_3O_4-III were produced by treating Co@C-II and Co-Co_3O_4@C-II in air at 550 ℃ for 1 h. Co_3O_4-II@graphite oxide (GO) and Co_3O_4-III@GO were also prepared to aid in evaluating the properties of Co_3O_4@C (the preparation procedure is shown in the Electronic Supplementary Material (ESM)).

2.3 Characterization

High-resolution transmission electron microscopy (HRTEM) and high-angle annular dark-field scanning transmission electron microscopy (HAADF-STEM) (HAADF) images of the as-prepared products were acquired on a FEI Tecnai G^2 F20 S-TWIN electron microscope at 200 kV. The phase structure of the as-prepared product was characterized via X-ray powder diffraction (XRD, Bruker D8 advance with Cu Kα, λ = 1.5418 Å). The average Co NP crystallite size was estimated via the Scherrer formula

$$D_h = \lambda/(\beta_h \cdot \cos \theta_h) \quad (1)$$

where D_h is the domain size of the diffraction line, λ is the wavelength of the Cu Kα source used, β_h is the width in radians of the diffraction peak measured at half-maximum intensity (fwhm, full width at half maximum) and corrected for instrumental broadening, and θ_h is the angle of the particular (*hkl*) reflection. Raman spectra were recorded on a Renishaw RM-1000 with excitation from the 514 nm line of an Ar-ion laser with a power of about 5 mW. X-ray photoelectron spectra (XPS) were recorded on a PHI quantera SXM

spectrometer with an Al Kα = 280.00 eV excitation source, and binding energies were calibrated by referencing the C1s peak (284.8 eV) to reduce the sample charge effect. Magnetic hysteresis (M–H) curves were measured on a Physical Property Measurement System (PPMS–9T) at 300 K with an applied magnetic field (H_{max} = 40 kOe). N_2 sorption isotherms were measured on an ASAP 2420 Surface Area and Porosity Analyzer at 77 K. Prior to measurement, the samples were degassed under high vacuum for 4 h at 523 K. The specific surface areas (S_{BET}) were obtained by applying the Brunauer–Emmett–Teller (BET) model to the portions of the adsorption branches of isotherms where P/P_0 was between 0.05 and 0.35. The pore size distributions were evaluated using the Barrett–Joyner–Halenda (BJH) model.

2.4 Catalytic hydrogen generation

The catalyst (20 mg) and $NaBH_4$ (80 mg) were placed in a round-bottomed glass flask. Then, NaOH (1 g) was dissolved in H_2O (20 mL). The sodium hydroxide solution was added to the flask through a dropping funnel. The flask was immersed in a temperature-controlled water bath, which was placed on a magnetic stirrer with stirring rate of 500 rpm. Hydrogen generation was studied via the traditional water displacement method [36]. Specific hydrogen generation rate (r_B) was calculated using information from the stabilizing stages (140 mL of hydrogen generated) according the following formula

$$r_B = \frac{140\ (\text{mL})}{t_{140}(\text{min})\ \omega_c(\text{g})} \quad (2)$$

where t_{140} is the time required to generate 140 mL of hydrogen, and w_c represents the mass of Co in the catalyst.

2.5 Recyclability tests

After the first cycle of hydrogen generation was completed, the catalysts were attracted to the bottom of the flask using a magnet, and the supernatant solution was removed. The separated catalysts were washed using water several times, dried and activated in air at 200 ℃ for 22 h. The catalytic hydrogen generation process was repeated 5 times.

3 Results and discussion

The synthesis strategy used to produce 3D core–shell Co-Co_3O_4@C is depicted in Scheme 1. The composite products are formed via precipitation and hydrothermal reaction, followed by annealing and thermal activation. During precipitation, Co-MOF nanocrystals are fabricated from cobalt nitrite and 2-methylimidazole in the presence of triethylamine. In the subsequent hydrothermal process, glucose carbonization is performed to generate a glucose polymer layer around the Co-MOF nanocrystals, resulting in Co-MOF@GP core–shell composites. After pyrolysis via annealing in a furnace with flowing nitrogen gas, Co@C is produced via thermally induced decomposition of Co-MOF nanocrystals to form Co NPs and carbon shells, and simultaneous carbonization of the glucose polymer. Furthermore, activation encourages cobalt NPs to partially transform in to Co_3O_4 layers. Thus, Co-Co_3O_4@C 3D core–shell composites are generated.

The morphologies and structural evolutions of the composite materials were investigated via transmission electron microscope (TEM) imaging. The resulting Co-MOF@GP contains a core–shell structure with spherical nanocrystals as the cores and amorphous carbon as the shells (Fig. 1(a)). The core diameters

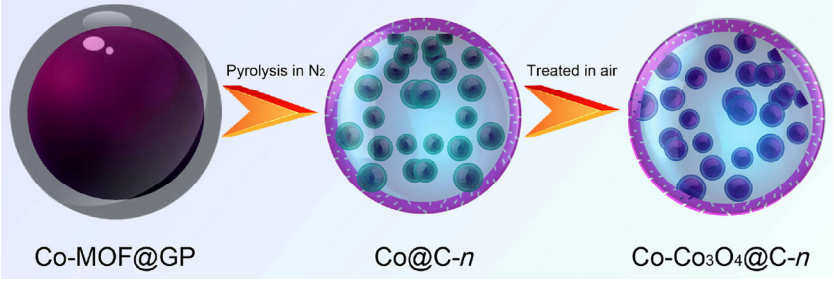

Scheme 1 Structural evolution of Co-MOF@GP to form Co-Co_3O_4@C-n.

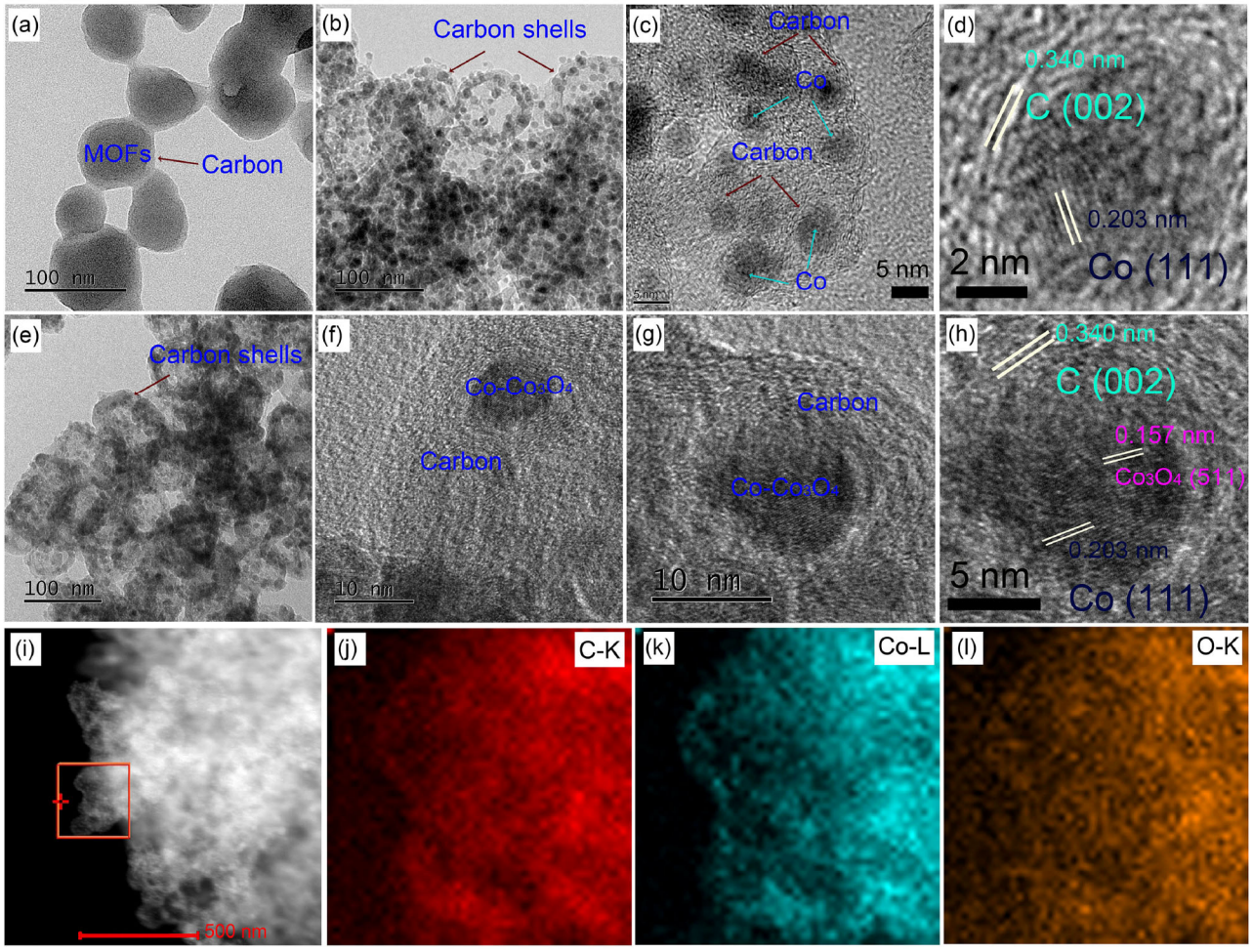

Figure 1 TEM images of (a) Co-MOF@GP, (b)–(d) Co@C-II, and (e)–(h) Co-Co_3O_4@C-II, (i) high-resolution HAADF-STEM image, and (j)–(l) EDX-STEM element mapping images of Co-Co_3O_4@C-II.

are in the range of 30–90 nm, and the carbon shell thicknesses are in the range of 4–8 nm (Fig. 1(a)). After pyrolysis at various temperatures, the resulting Co@C-*n* is composed of several hollow carbon spheres, which are interconnected via graphitic carbon layers (Fig. 1(b), and Figs. S1(a) and S1(g) in the ESM). Each hollow carbon sphere contains several well-dispersed Co NPs encapsulated in carbon matrices. These Co NPs are derived from the pyrolysis of Co-MOF nanocrystals. The diameters of the Co NPs in Co@C-II range from 4 to 14 nm (Fig. 1(b)). The configuration of Co@C-*n* is confirmed via HRTEM imaging (Figs. 1(c) and 1(d), and Figs. S1(b)–1(c) and S1(h)–1(i) in the ESM). The Co cores and carbon shells inside the hollow carbon spheres are observed clearly. Co-Co_3O_4@C-*n* exhibit similar morphology to that of Co@C-*n* (Fig. 1(e) and Figs. S1(d) and S1(j) in the ESM). After activation, cobalt NPs partially transform into Co_3O_4, as verified via XRD pattern analysis. The configuration of Co-Co_3O_4@C-*n* is determined using detailed HRTEM images (Figs. 1(f)–1(h) and Figs. S1(e), S1(f), S1(k), S1(l), and S1(h) in the ESM). Energy dispersive X-ray spectroscopy (EDX) of Co-Co_3O_4@C-II identifies the uniform distributions of C, Co, and O, which demonstrate oxidation of Co NPs during activation (Figs. 1(i)–1(l)).

Various diffraction features are observed in the XRD patterns of Co-MOF, Co-MOF@GP, Co@C-II, and Co-Co_3O_4@C-II (Fig. 2(a)). As expected, the diffraction peak positions in Co-MOF@GP correspond to XRD patterns simulated from single crystal structures of ZIF-67, confirming the formation and presence of

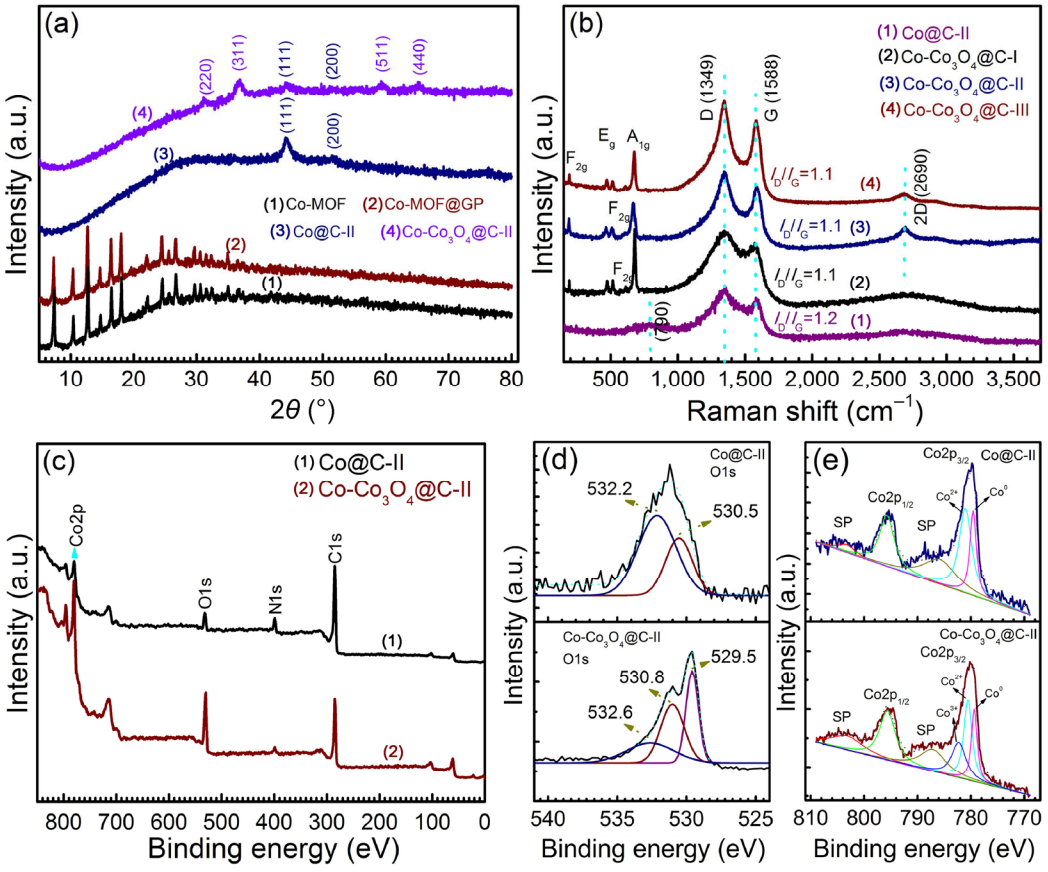

Figure 2 (a) XRD patterns of as-synthesized Co-MOF, Co-MOF@GP, Co@C-II, and Co-Co_3O_4@C-II, (b) Raman spectra of Co@C-II and Co-Co_3O_4@C-*n*, (c) full XPS, and (d)–(e) O1s and Co2p XPS of Co@C-II and Co-Co_3O_4@C-II.

Co-MOF in the self-assembled hybrid [35, 37]. The XRD pattern of Co-MOF@GP does not exhibit any other peaks, indicating that the crystalline order of the Co-MOF host matrix remains unchanged after coating with GP. This is due to the formation of amorphous carbon during hydrothermal treatment of Co-MOF and glucose. The diffraction peaks of Co@C-II reveal the presence of Co and graphitic C. The broadened peaks at around 25° (2θ) are attributed to graphitic C (002) lattice facets. The peaks at 44.2° and 51.5° are ascribed to the (111) and (200) lattice facets of cubic β-Co (JCPDS card no. 89-4307) [34, 38]. The XRD pattern of Co-Co_3O_4@C-II contains additional peaks at 31.2°, 36.8°, 59.3°, and 65.2°. These additional peaks correspond to the (220), (311), (511), and (440) lattice facets of the pure cubic spinel phase of Co_3O_4 (JCPDS card no. 42-1467), respectively [39]. This result indicates the coexistence of Co and Co_3O_4 NPs in Co-Co_3O_4@C-II. Co NPs are partially oxidized and converted into Co_3O_4. Co@C-I and Co@C-III exhibit patterns similar to those of Co@C-II, meanwhile Co-Co_3O_4@C-I and Co-Co_3O_4@C-III exhibit patterns similar to those of Co-Co_3O_4@C-II, except for the XRD peak intensities (Figs. S2(a) and S2(b) in the ESM). The diffraction peaks enlarge and sharpen when samples are calcined at elevated temperatures. More detailed structural information about the material was provided via Raman spectroscopy analysis (Fig. 2(b) and Fig. S3 in the ESM). The D bands at about 1,349 cm^{-1} and G bands at about 1,588 cm^{-1} are clearly observed in the spectra of Co@C-*n* and Co-Co_3O_4@C-*n*. They demonstrate the presence of carbonaceous content, which can be attributed to the pyrolysis of Co-MOF and carbonization of glucose [40]. The calculated I_D/I_G intensity ratios of Co@C-*n* and Co-Co_3O_4@C-*n* are 1.2 and 1.1, respectively, and are typical of disordered graphitic carbons. The 2D bands around 2,690 cm^{-1} suggest that there are several carbon layers in Co@C-III,

Co-Co_3O_4@C-II and Co-Co_3O_4@C-III. The weak, wide band around 790 cm^{-1} in Co@C-*n* is assigned to the CoO_x surface species (Fig. 2(b) and Fig. S3 in the ESM). Several bands at 192, 472, 519, 608, and 680 cm^{-1} are also detected in the spectrum of Co-Co_3O_4@C-*n*, and are assigned to the five Raman-active modes (F_{2g}, E_g, F_{2g}, F_{2g}, and A_{1g}) caused by the presence of Co_3O_4 [41].

The full survey XPS of Co@C-II and Co-Co_3O_4@C-II confirm the presence of carbon, cobalt, nitrogen, and oxygen surface species (Fig. 2(c)). The relative atomic ratios of N, C, O, and Co in Co@C-II and Co-Co_3O_4@C-II were calculated from the XPS (Table S1 in the ESM). The improved O content indicates surface oxidation of Co. The C1s spectrum of Co@C-II can be fitted to three peaks. The peaks at 284.4, 285.1, and 287.5 eV are ascribed to the C=C bond, and C–C and C=O groups, respectively [42]. The C1s spectrum of Co-Co_3O_4@C-II is similar to that of Co@C-II. The peaks at 284.4, 285.1, and 287.0 eV correspond to C=C, C–C, and C=O bonds, respectively (Figs. S4(a) and S4(b) in the ESM). Elemental analysis was used to determine that the C concentrations were 37%, 48%, 50%, 30%, 42%, and 44% in Co@C-I, Co@C-II, Co@C-III, Co-Co_3O_4@C-I, Co-Co_3O_4@C-II, and Co-Co_3O_4@C-III, respectively (Table S2 in the ESM). The O1s spectrum of Co@C-II can be identified by two peaks: –OH (530.5 eV), and absorbed water (532.2 eV) [43]. While an additional peak Co=O (529.5 eV) is present in the O1s spectrum of Co-Co_3O_4@C-II, the peaks of –OH (530.8 eV) and absorbed water (532.7 eV) still exist, demonstrating that the Co NPs partially convert into Co_3O_4 after activation in air at 200 ℃ (Fig. 2(d)). The Co2p spectrum of Co@C-II can be fitted to several peaks. The peaks around 778.8 eV are assigned to Co^0 [44]. The peaks at 781.1 eV ($Co2p_{3/2}$) and 795.6 eV ($Co2p_{1/2}$) are attributed to Co^{2+}, which is produced by surface oxidation of the samples. The peaks at 786.2 and 803.4 eV are shake-up satellite peaks [45, 46]. An additional peak from Co^{3+} (782.2 eV) appears in the Co2p spectrum of Co-Co_3O_4@C-II [47–49], which is companied by the Co^0 (778.8 eV), Co^{2+} (780.6 eV for $Co2p_{3/2}$, 795.6 eV for $Co2p_{1/2}$), and shake-up satellite peaks (787.4 and 803.4 eV). This proves that Co NPs partially convert into Co_3O_4 after activation in air at 200 ℃ (Fig. 2(e)). Based on results from calcination in air and thermal gravity analysis (TGA) results from the samples, the mass ratios of Co are calculated to be 30.8%, 36.7%, 37.5%, 36.1%, 41.1%, and 39.4% for Co@C-I, Co@C-II, Co@C-III, Co-Co_3O_4@C-I, Co-Co_3O_4@C-II, and Co-Co_3O_4@C-III, respectively (Fig. S5 in the ESM) [50]. The similar N1s region spectra of Co@C-II and Co-Co_3O_4@C-II are fitted to three peaks. The peaks at 398.8 eV are related to pyridinic–N bonds, the peaks at about 400.3 eV represent the contribution from pyrrolic–N bonds, and the peaks around 403 eV are attributed to oxidized nitrogen in carbon shells (Figs. S6(a) and S6(b) in the ESM) [51–53]. The high pyridinic–N content of the carbon shells benefits the catalytic activities of the metallic components [15].

Nitrogen adsorption–desorption isotherms measured at 77 K were used to evaluate the specific surface areas and porous structures of Co-Co_3O_4@C-*n*. The samples exhibit type-IV isotherms with hysteresis loops, indicating the presence of mesoporous structures (Fig. 3(a)) [54, 55]. The S_{BET} of Co-Co_3O_4@C-I, Co-Co_3O_4@C-II, and Co-Co_3O_4@C-III are 153, 185, and 227 $m^2 \cdot g^{-1}$, respectively. These relatively high specific surface areas are beneficial during catalysis. These porosities were confirmed again via pore distribution analysis (Fig. 3(b)). Co-Co_3O_4@C-*n* possesses not only mesopores with a predominant diameter of 4 nm, but some meso-macro porosity at about 39–82 nm. These porous structures aid in mass transfer of substrates and products during catalytic reactions.

It was interesting to explore the potential applications and magnetic properties of the Co@C-*n* and Co-Co_3O_4@C-*n* nanocomposites. All samples exhibit typical ferromagnetic behavior at 300 K due to the presence of Co NPs (Fig. 4). The saturation magnetization (M_s) values of Co@C-I, Co@C-II, Co@C-III, Co-Co_3O_4@C-I, Co-Co_3O_4@C-II, and Co-Co_3O_4@C-III are 71.2, 80.1, 103.7, 8.8, 23.8, and 49.3 emu·g_{Co}^{-1}, respectively (Fig. 4(a)). The low M_s of Co-Co_3O_4@C-*n* is ascribed primarily to the formation of Co_3O_4 NPs after activation in air. This is corroborated by XRD, Raman, and XPS analysis. No hysteresis loops were observed for Co@C-I and Co-Co_3O_4@C-I, indicating super-paramagnetic behavior without permanent magnetic moment. The *M*–*H* curves of Co@C-II, Co@C-III, Co-Co_3O_4@C-II, and Co-Co_3O_4@C-III display representative hysteresis loops. The coercivity (H_c) and remanence (M_r) are 206 Oe, 10.4 emu·g_{Co}^{-1}; 343 Oe,

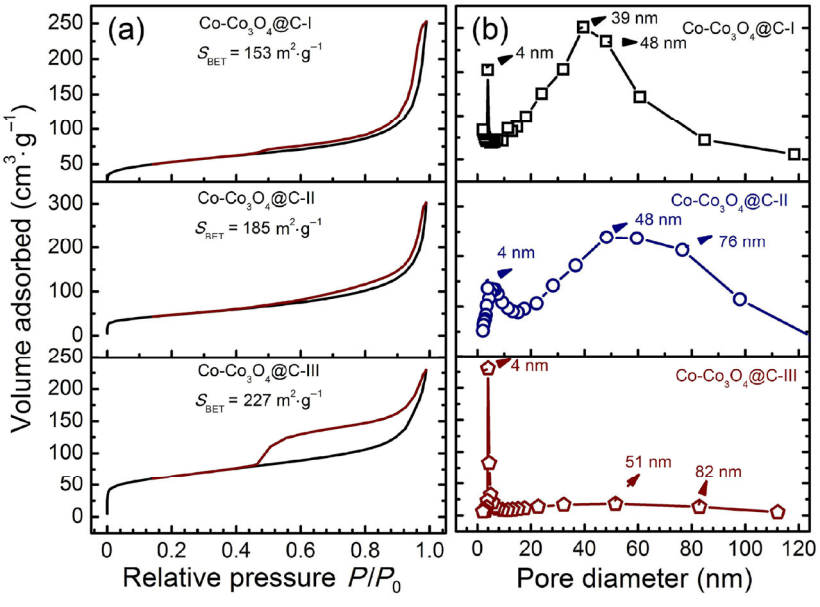

Figure 3 (a) N_2 adsorption−desorption isotherms and (b) pore-size distribution of Co-Co_3O_4@C-*n*.

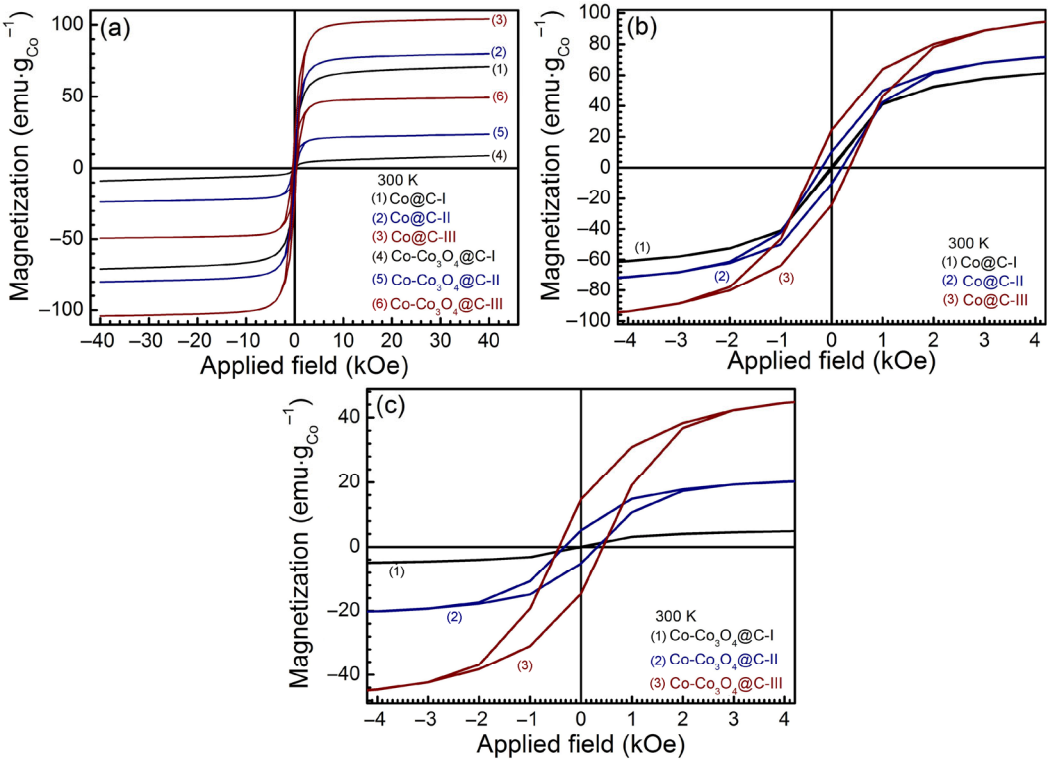

Figure 4 (a) *M*–*H* curves of Co@C-*n* and Co-Co_3O_4@C-*n*, (b)–(c) enlarged views.

24.1 emu·g_{Co}^{-1}; 320 Oe, 5.1 emu·g_{Co}^{-1}; and 430 Oe and 14.4 emu·g_{Co}^{-1}, respectively (Figs. 4(b) and 4(c)). These characteristics, which are typical of ferromagnetism, aid in the effective magnetic separation of catalysts from the reaction system and magnetic momentum transfer in batch or continuous flow reactors (Fig. S7 in the ESM) [31−33, 56, 57].

The catalytic activities of as-prepared samples during hydrolysis of $NaBH_4$ solution were investigated using a batch reactor. As in our previous reports,

the hydrogen generation reaction was conducted at 500 RPM in self-stirring mode [31–33]. A simplified diagram of the batch reactor and stirring mechanism are displayed in Fig. S8 in the ESM. First, the hydrogen generation reaction takes place with various samples used as catalysts at 298 K (Fig. 5(a)). The r_B of Co@C-I and Co-Co_3O_4@C-I, Co@C-II and Co-Co_3O_4@C-II, Co@C-III and Co-Co_3O_4@C-III are 455 and 2,100, 1,370 and 5,360, 1,950 and 2,990 mL·min^{-1}·g_{Co}^{-1}, respectively. The Co-Co_3O_4@C-*n* sample exhibits a higher specific r_B than the corresponding Co@C-*n* and Co_3O_4@C samples (Fig. 5(b)). The excellent catalytic performance of Co-Co_3O_4@C-*n* may be attributed to the coexistence of Co and Co_3O_4 NPs inside the carbon shells. To explore the catalytic properties of the samples, Co@C-II was treated in air at various temperatures and for various durations. Variations on Co-Co_3O_4@C are produced when Co@C-II is treated at 100 ˚C for 22 h, or at 200 ˚C for 11 h or 44 h (Figs. S9(a)–9(c) in the ESM). In contrast, porous Co_3O_4-I is obtained when Co@C-II is treated at 300 ˚C for 22 h (Fig. S9(d) in the ESM). The XRD patterns suggest that partial oxidation can be performed

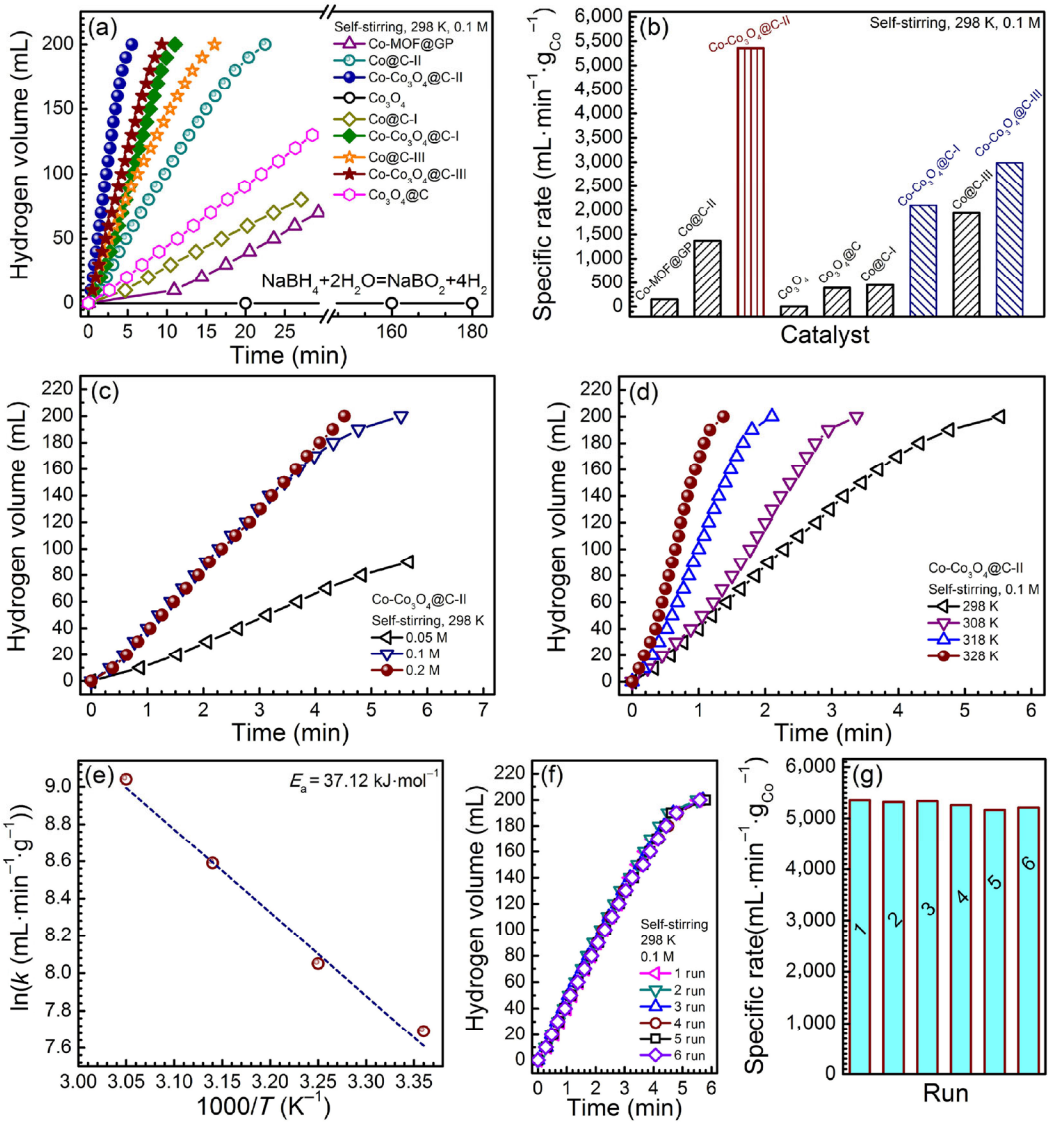

Figure 5 (a)–(b) Hydrogen generation via hydrolysis of $NaBH_4$, catalyzed by various materials at 298 K and the corresponding comparison of hydrogen generation rates by catalyst, catalytic hydrogen generation with Co-Co_3O_4@C-II (c) at various $NaBH_4$ concentrations, (d)–(e) at various temperatures (and corresponding Arrhenius plot), (f)–(g) stability test with Co-Co_3O_4@C-II at 298 K and the corresponding rates of hydrogen generation with Co-Co_3O_4@C-II during each cycle.

successfully in all tested conditions except treatment at 300 ℃ for 22 h (Fig. S10(a) in the ESM). The best hydrogen production is achieved when the samples are prepared at 200 ℃ for 22 h (Co-Co_3O_4@C-II) (Fig. S10(b) in the ESM). In addition, treatment of Co@C-II and Co-Co_3O_4@C-II in air at 550 ℃ for 1 h produces porous Co_3O_4-II and Co_3O_4-III (Fig. S11 in the ESM). Co_3O_4-II@GO and Co_3O_4-III@GO were also prepared to test the properties of Co_3O_4@C (Fig. S12 in the ESM, for the preparation procedure). The XRD patterns confirm the formation of Co_3O_4 and Co_3O_4@GO (Fig. S13(a) in the ESM). Co_3O_4@C exhibits better catalytic activity than pure Co_3O_4 (Fig. S13(b) in the ESM). Regardless, the catalytic activities of Co-Co_3O_4@C are much higher than those of Co@C and Co_3O_4@C (Figs. S13(c) and S13(d) in the ESM). The excellent catalytic performance of Co-Co_3O_4@C may be ascribed to synergistic effects from Co and Co_3O_4 NPs.

The kinetics of hydrolysis is dependent on catalytic activity and other factors. Varying the initial $NaBH_4$ concentration causes different effects on the performances of different catalysts. The r_B of Co-Co_3O_4@C-II decreases when the $NaBH_4$ concentration is 0.05 M, but is not influenced by higher concentrations (0.1 and 0.2 M) (Fig. 5(c)). This may be because mass transfer is a limiting factor at low $NaBH_4$ concentrations. The catalysts significantly enhance the reaction kinetics when high-concentration substrates are used [58]. The r_B of Co-Co_3O_4@C-II clearly increases with the temperature because of faster movement by BH_4^- ions and water molecules (Fig. 5(d)). As expected, the Arrhenius plot of ln k vs. the reciprocal of the absolute temperature ($1/T$) is a straight line (Fig. 5(e)). The Arrhenius energy (E_a) of the catalytic reaction can be calculated using the following Arrhenius equation

$$k_0 = A\exp\left(-\frac{E_a}{RT}\right) \quad (3)$$

where k_0 denotes the rate constant, A is the pre-exponential factor, R represents the ideal gas constant, and T is the reaction temperature. The slope of the Arrhenius plot provides the activation energy (E_a = 37.12 kJ·mol^{-1}). This value is lower than those reported with other Co-based catalysts [59–61]. The relatively low Arrhenius energy may originate from synergistic interactions between Co_3O_4 and Co NPs. For a clear comparison, the maximum r_B and E_a of other metal catalysts are listed in Table S3 (in the ESM).

The stability of Co-Co_3O_4@C-n after recycling was evaluated via hydrolysis of $NaBH_4$. The XRD pattern reveals that Co and Co_3O_4 coexist in the reused catalysts (Fig. S14 in the ESM). The catalyst Co-Co_3O_4@C-II exhibits superior stability, nearly maintaining its initial activity after being used up to six times (97.4% of r_B in first run) (Figs. 5(f) and 5(g)). This recycling stability is better than those of highly active Co-based catalysts reported in Refs. [29–33]. The core–shell nanostructure of Co-Co_3O_4@C-II is preserved well after being used six times for hydrolysis of $NaBH_4$ (Fig. S15 in the ESM). The efficient catalytic properties of Co-Co_3O_4@C-II may be caused by synergic effects between Co-Co_3O_4 NPs and carbon shells. The carbon shells coated onto Co-Co_3O_4 NPs isolate the Co-Co_3O_4 NPs from each other on carbon films and large surfaces (Figs. 1 and 3). The relatively high surface areas are also responsible for catalytic reactions. They provide more active sites with easy mass transfer. Precise identification of the active phase in Co-based catalytic hydrolysis of $NaBH_4$ is a very complex challenge due to *in situ* characterization difficulties [62]. Generally, a core–shell composite structure of cobalt-cobalt oxide-(poly) borates forms in the initial stage of a catalytic reaction [63, 64]. The amorphous state of the surface region and presence of boron in the surface species are requirements for high catalytic activity in Co-based catalysts. Based on above hypothesis, the Co-Co_3O_4 heterojunctions provide a satisfactory surface precursor for *in situ* formation of possible catalytically active phases ($2CoO{\cdot}B_2O_4{\cdot}4H_2O$ or $Co@B_\alpha O_\beta(OH)_\gamma$) [64, 65]. Some control experiments were conducted by leaching Co@C-n and Co-Co_3O_4@C-n with HCl to verify the process of diffusion through the carbon shells during the catalytic reaction. The graphitic carbon layer is inert to leaching with HCl. Photographic images of the acid leaching process are provided (Fig. S16 in the ESM). A pink solution is obtained after acid leaching. The pink color is likely due to the presence of Co^{2+} ions in solution. Protons and Co^{2+} diffuse freely through the carbon layer, which indicates that there are some pores in the carbon layer shells. These pores allow diffusion of the substrate and product molecules during catalysis.

4 Conclusions

Hollow carbon sphere-wrapped Co NPs@C core–shell composites were constructed via pyrolysis of glucose polymer-wrapped Co-MOF nanocrystals synthesized via an *in situ* hydrothermal treatment. Thermal treatment in air tuned the composition of Co NPs@C by converting some Co^0 to Co_3O_4 and forming heterojunctions. These Co-Co_3O_4 heterojunctions in the nanoparticle cores provided very high catalytic activities for hydrogen generation via hydrolysis of $NaBH_4$. The carbon shells protected the Co-Co_3O_4 cores from leaching, aggregating, and growing. Superior catalytic performance, including high activity and excellent stability were obtained. This method of fabricating and pyrolyzing core–shell MOF composites in confined spaces for construction of hierarchical core–shells with heterojunctions may have broad applications in areas of electro- or chemical catalysis that involve energy storage and conversion.

Acknowledgements

Financial supports from the National Natural Science Foundation of China (Nos. 21371154, 21401168, and U1204203) are acknowledged.

Electronic Supplementary Material: Supplementary material (experimental details and some characterization results) is available in the online version of this article at https://doi.org/10.1007/s12274-017-1519-1.

References

[1] Wu, R. B.; Wang, D. P.; Rui, X. H.; Liu, B.; Zhou, K.; Law, A. W. K.; Yan, Q. Y.; Wei, J.; Chen, Z. *In-situ* formation of hollow hybrids composed of cobalt sulfides embedded within porous carbon polyhedra/carbon nanotubes for high-performance lithium-ion batteries. *Adv. Mater.* **2015**, *27*, 3038–3044.

[2] Amali, A. J.; Hoshino, H.; Wu, C.; Ando, M.; Xu, Q. From metal–organic framework to intrinsically fluorescent carbon nanodots. *Chem.—Eur. J.* **2014**, *20*, 8279–8282.

[3] Cho, W.; Park, S.; Oh, M. Coordination polymer nanorods of Fe-MIL-88B and their utilization for selective preparation of hematite and magnetite nanorods. *Chem. Commun.* **2011**, *47*, 4138–4140.

[4] Aiyappa, H. B.; Pachfule, P.; Banerjee, R.; Kurungot, S. Porous carbons from nonporous MOFs: Influence of ligand characteristics on intrinsic properties of end carbon. *Cryst. Growth Des.* **2013**, *13*, 4195–4199.

[5] Tang, J.; Salunkhe, R. R.; Liu, J.; Torad, N. L.; Imura, M.; Furukawa, S.; Yamauchi, Y. Thermal conversion of core–shell metal–organic frameworks: A new method for selectively functionalized nanoporous hybrid carbon. *J. Am. Chem. Soc.* **2015**, *137*, 1572–1580.

[6] Srinivas, G.; Krungleviciute, V.; Guo, Z. X.; Yildirim, T. Exceptional CO_2 capture in a hierarchically porous carbon with simultaneous high surface area and pore volume. *Energy Environ. Sci.* **2014**, *7*, 335–342.

[7] Jia, Y.; Sun, C. H.; Peng, Y.; Fang, W. Q.; Yan, X. C.; Yang, D. J.; Zou, J.; Mao, S. S.; Yao, X. D. Metallic Ni nanocatalyst *in situ* formed from a metal–organic-framework by mechanochemical reaction for hydrogen storage in magnesium. *J. Mater. Chem. A* **2015**, *3*, 8294–8299.

[8] Huang, G.; Zhang, F. F.; Du, X. C.; Qin, Y. L.; Yin, D. M.; Wang, L. M. Metal organic frameworks route to *in situ* insertion of multiwalled carbon nanotubes in Co_3O_4 polyhedra as anode materials for lithium-ion batteries. *ACS Nano* **2015**, *9*, 1592–1599.

[9] Liu, J. Y.; Yan, J.; Ji, H. Y.; Xu, Y. G.; Huang, L. Y.; Li, Y. P.; Song, Y. H.; Zhang, Q.; Xu, H.; Li, H. M. Controlled synthesis of ordered mesoporous g-C_3N_4 with a confined space effect on its photocatalytic activity. *Mater. Sci. Semicon. Proc.* **2016**, *46*, 59–68.

[10] Manna, P.; Debgupta, J.; Bose, S.; Das, S. K. A mononuclear Co^{II} coordination complex locked in a confined space and acting as an electrochemical water-oxidation catalyst: A "ship-in-a-bottle" approach. *Angew. Chem., Int. Ed.* **2016**, *55*, 2425–2430.

[11] Fei, L. F.; Li, X. G.; Bi, W. T.; Zhuo, Z. W.; Wei, W. F.; Sun, L.; Lu, W.; Wu, X. J.; Xie, K. Y.; Wu, C. Z. et al. Graphene/sulfur hybrid nanosheets from a space-confined "Sauna" reaction for high-performance lithium–sulfur batteries. *Adv. Mater.* **2015**, *27*, 5936–5942.

[12] Xu, S. K.; Zhang, P.; Li, H. B.; Wei, H. J.; Li, L. M.; Li, B. J.; Wang, X. Y. Ru nanoparticles confined in carbon nanotubes: Supercritical CO_2 assisted preparation and improved catalytic performances in hydrogenation of D-glucose. *RSC Adv.* **2014**, *4*, 7079–7083.

[13] Zou, F.; Chen, Y. P.; Liu, K. W.; Yu, Z. T.; Liang, W. F.; Bhaway, S. M.; Gao, M.; Zhu, Y. Metal organic frameworks derived hierarchical hollow NiO/Ni/graphene composites for lithium and sodium storage. *ACS Nano* **2016**, *10*, 377–386.

[14] Chen, Y. H.; Kanan, M. W. Tin oxide dependence of the CO_2 reduction efficiency on tin electrodes and enhanced

activity for tin/tin oxide thin-film catalysts. *J. Am. Chem. Soc.* **2012**, *134*, 1986–1989.

[15] Bi, Q. Y.; Lin, J. D.; Liu, Y. M.; He, H. Y.; Huang, F. Q.; Cao, Y. Dehydrogenation of formic acid at room temperature: Boosting palladium nanoparticle efficiency by coupling with pyridinic nitrogen-doped carbon. *Angew. Chem., Int. Ed.* **2016**, *55*, 11849–11853.

[16] Xia, W.; Zou, R. Q.; An, L.; Xia, D. G.; Guo, S. J. A metal–organic framework route to *in situ* encapsulation of Co@Co_3O_4@C core@bishell nanoparticles into a highly ordered porous carbon matrix for oxygen reduction. *Energy Environ. Sci.* **2015**, *8*, 568–576.

[17] Gao, S.; Lin, Y.; Jiao, X. C.; Sun, Y. F.; Luo, Q. Q.; Zhang, W. H.; Li, D. Q.; Yang, J. L.; Xie, Y. Partially oxidized atomic cobalt layers for carbon dioxide electroreduction to liquid fuel. *Nature* **2016**, *529*, 68–71.

[18] Wu, G. P.; Wang, J.; Ding, W.; Nie, Y.; Li, L.; Qi, X. Q.; Chen, S. G.; Wei, Z. D. A strategy to promote the electrocatalytic activity of spinels for oxygen reduction by structure reversal. *Angew. Chem., Int. Ed.* **2016**, *55*, 1340–1344.

[19] Wang, J.; Zhong, H. X.; Wang, Z. L.; Meng, F. L.; Zhang, X. B. Integrated three-dimensional carbon paper/carbon tubes/cobalt-sulfide sheets as an efficient electrode for overall water splitting. *ACS Nano* **2016**, *10*, 2342–2348.

[20] Wang, J.; Zhang, X. B.; Wang, Z. L.; Wang, L. M.; Zhang, Y. Rhodium-nickel nanoparticles grown on graphene as highly efficient catalyst for complete decomposition of hydrous hydrazine at room temperature for chemical hydrogen storage. *Energy Environ. Sci.* **2012**, *5*, 6885–6888.

[21] Wang, J.; Qin, Y. L.; Liu, X.; Zhang, X. B. *In situ* synthesis of magnetically recyclable graphene-supported Pd@Co core–shell nanoparticles as efficient catalysts for hydrolytic dehydrogenation of ammonia borane. *J. Mater. Chem.* **2012**, *22*, 12468–12470.

[22] Qin, Y. L.; Wang, J.; Meng, F. Z.; Wang, L. M.; Zhang, X. B. Efficient PdNi and PdNi@Pd-catalyzed hydrogen generation via formic acid decomposition at room temperature. *Chem. Commun.* **2013**, *49*, 10028–10030.

[23] Wang, Z. L.; Hao, X. F.; Jiang, Z.; Sun, X. P.; Xu, D.; Wang, J.; Zhong, H. X.; Meng, F. L.; Zhang, X. B. C and N hybrid coordination derived Co-C-N complex as a highly efficient electrocatalyst for hydrogen evolution reaction. *J. Am. Chem. Soc.* **2015**, *137*, 15070–15073.

[24] Zhou, L. M.; Zhang, T. R.; Tao, Z. L.; Chen, J. Ni nanoparticles supported on carbon as efficient catalysts for the hydrolysis of ammonia borane. *Nano Res.* **2014**, *7*, 774–781.

[25] Yan, J. M.; Zhang, X. B.; Akita, T.; Haruta, M.; Xu, Q. One-step seeding growth of magnetically recyclable Au@Co core–shell nanoparticles: Highly efficient catalyst for hydrolytic dehydrogenation of ammonia borane. *J. Am. Chem. Soc.* **2010**, *132*, 5326–5327.

[26] Zhu, J.; Li, R.; Niu, W. L.; Wu, Y. J.; Gou, X. L. Facile hydrogen generation using colloidal carbon supported cobalt to catalyze hydrolysis of sodium borohydride. *J. Power Sources* **2012**, *211*, 33–39.

[27] Lu, A. L.; Chen, Y. Z.; Jin, J. R.; Yue, G. H.; Peng, D. L. CoO nanocrystals as a highly active catalyst for the generation of hydrogen from hydrolysis of sodium borohydride. *J. Power Sources* **2012**, *220*, 391–398.

[28] Niu, W. L.; Ren, D. B.; Han, Y. Y.; Wu, Y. J.; Gou, X. L. Optimizing preparation of carbon supported cobalt catalyst for hydrogen generation from $NaBH_4$ hydrolysis. *J. Alloys Compd.* **2012**, *543*, 159–166.

[29] Zhang, H.; Ling, T.; Du, X. W. Gas-phase cation exchange toward porous single-crystal CoO nanorods for catalytic hydrogen production. *Chem. Mater.* **2015**, *27*, 352–357.

[30] Mahmood, J.; Jung, S. M.; Kim, S. J.; Park, J.; Yoo, J. W.; Baek, J. B. Cobalt oxide encapsulated in C_2N-*h*2D network polymer as a catalyst for hydrogen evolution. *Chem. Mater.* **2015**, *27*, 4860–4864.

[31] Liu, Y. Y.; Zhang, J.; Zhang, X. J.; Li, B. J.; Wang, X. Y.; Cao, H. Q.; Wei, D.; Zhou, Z. F.; Cheetham, A. K. Magnetic catalysts as nanoactuators to achieve simultaneous momentum-transfer and continuous-flow hydrogen production. *J. Mater. Chem. A* **2016**, *4*, 4280–4287.

[32] Xing, C. C.; Liu, Y. Y.; Su, Y. H.; Chen, Y. H.; Hao, S.; Wu, X. L.; Wang, X. Y.; Cao, H. Q.; Li, B. J. Structural evolution of Co-based metal organic frameworks in pyrolysis for synthesis of core–shells on nanosheets: Co@CoO_x@carbon-rGO composites for enhanced hydrogen generation activity. *ACS Appl. Mater. Interfaces* **2016**, *8*, 15430–15438.

[33] Duan, S. S.; Han, G. S.; Su, Y. H.; Zhang, X. Y.; Liu, Y. Y.; Wu, X. L.; Li, B. J. Magnetic Co@g-C_3N_4 core–shells on rGO sheets for momentum transfer with catalytic activity toward continuous-flow hydrogen generation. *Langmuir* **2016**, *32*, 6272–6281.

[34] Yu, G. L.; Sun, J.; Muhammad, F.; Wang, P. Y.; Zhu, G. S. Cobalt-based metal organic framework as precursor to achieve superior catalytic activity for aerobic epoxidation of styrene. *RSC Adv.* **2014**, *4*, 38804–38811.

[35] Banerjee, R.; Phan, A.; Wang, B.; Knobler, C.; Furukawa, H.; O'Keeffe, M.; Yaghi, O. M. High-throughput synthesis of zeolitic imidazolate frameworks and application to CO_2 capture. *Science* **2008**, *319*, 939–943.

[36] Rong, C. B.; Poudyal, N.; Chaubey, G. S.; Nandwana, V.; Liu, Y.; Wu, Y. Q.; Kramer, M. J.; Kozlov, M. E.; Baughman, R. H.; Liu, J. P. High thermal stability of carbon-coated $L1_0$-FePt nanoparticles prepared by salt-matrix annealing. *J. Appl. Phys.* **2008**, *103*, 07E131.

[37] Qian, J. F.; Sun, F. A.; Qin, L. Z. Hydrothermal synthesis of zeolitic imidazolate framework-67 (ZIF-67) nanocrystals. *Mater. Lett.* **2012**, *82*, 220–223.

[38] Zhou, Y. X.; Chen, Y. Z.; Cao, L. N.; Lu, J. L.; Jiang, H. L. Conversion of a metal–organic framework to N-doped porous carbon incorporating Co and CoO nanoparticles: Direct oxidation of alcohols to esters. *Chem. Commun.* **2015**, *51*, 8292–8295.

[39] Lin, K. Y. A.; Hsu, F. K.; Lee, W. D. Magnetic cobalt-graphene nanocomposite derived from self-assembly of MOFs with graphene oxide as an activator for peroxymonosulfate. *J. Mater. Chem. A* **2015**, *3*, 9480–9490.

[40] Zhong, S.; Zhan, C. X.; Cao, D. P. Zeolitic imidazolate framework-derived nitrogen-doped porous carbons as high performance supercapacitor electrode materials. *Carbon* **2015**, *8*, 51–59.

[41] Liu, Y. W.; Xiao, C.; Lyu, M. J.; Lin, Y.; Cai, W. Z.; Huang, P. C.; Tong, W.; Zou, Y. M.; Xie, Y. Ultrathin Co_3S_4 nanosheets that synergistically engineer spin states and exposed polyhedra that promote water oxidation under neutral conditions. *Angew. Chem., Int. Ed.* **2015**, *54*, 11231–11235.

[42] Gao, S.; Li, G. D.; Liu, Y. P.; Chen, H.; Feng, L. L.; Wang, Y.; Yang, M.; Wang, D. J.; Wang, S.; Zou, X. X. Electrocatalytic H_2 production from seawater over Co, N-codoped nanocarbons. *Nanoscale* **2015**, *7*, 2306–2316.

[43] Liu, B.; Kong, D. Z.; Zhang, J.; Wang, Y.; Chen, T. P.; Cheng, C. W.; Yang, H. Y. 3D hierarchical Co_3O_4@Co_3S_4 nanoarrays as cathode materials for asymmetric pseudo-capacitors. *J. Mater. Chem. A* **2016**, *4*, 3287–3296.

[44] Yin, P. Q.; Yao, T.; Wu, Y. E.; Zheng, L. R.; Lin, Y.; Liu, W.; Ju, H. X.; Zhu, J. F.; Hong, X.; Deng, Z. X. et al. Single cobalt atoms with precise N-coordination as superior oxygen reduction reaction catalysts. *Angew. Chem., Int. Ed.* **2016**, *55*, 10800–10805.

[45] Wei, J.; Hu, Y. X.; Liang, Y.; Kong, B.; Zhang, J.; Song, J. C.; Bao, Q. L.; Simon, G. P.; Jiang, S. P.; Wang, H. T. Nitrogen-doped nanoporous carbon/graphene nano-sandwiches: Synthesis and application for efficient oxygen reduction. *Adv. Funct. Mater.* **2015**, *25*, 5768–5777.

[46] Huang, Y. C.; Ye, K. H.; Li, H. B.; Fan, W. J.; Zhao, F. Y.; Zhang, Y. M.; Ji, H. B. A highly durable catalyst based on $Co_xMn_{3-x}O_4$ nanosheets for low-temperature formaldehyde oxidation. *Nano Res.* **2016**, *9*, 3881–3892.

[47] Fu, L.; Liu, Z. M.; Liu, Y. Q.; Han, B. X.; Hu, P. G.; Cao, L. C.; Zhu, D. B. Beaded cobalt oxide nanoparticles along carbon nanotubes: Towards more highly integrated electronic devices. *Adv. Mater.* **2005**, *17*, 217–221.

[48] Kong, L. J.; Ren, Z. Y.; Zheng, N. N.; Du, S. C.; Wu, J.; Tang, J. L.; Fu, H. G. Interconnected 1D Co_3O_4 nanowires on reduced graphene oxide for enzymeless H_2O_2 detection. *Nano Res.* **2015**, *8*, 469–480.

[49] Shi, Q.; Wang, Y. D.; Wang, Z. M.; Lei, Y. P.; Wang, B.; Wu, N.; Han, C.; Xie, S.; Gou, Y. Z. Three-dimensional (3D) interconnected networks fabricated via *in-situ* growth of N-doped graphene/carbon nanotubes on Co-containing carbon nanofibers for enhanced oxygen reduction. *Nano Res.* **2016**, *9*, 317–328.

[50] Ingier-Stocka, E. TG and DTA evaluation of cobalt salts and complexes mixed with activated carbon. *J. Therm. Anal. Calorim.* **2001**, *65*, 561–573.

[51] Pu, J.; Li, C. W.; Tang, L.; Li, T. T.; Ling, L.; Zhang, K.; Xu, Y. C.; Li, Q. W.; Yao, Y. G. Impregnation assisted synthesis of 3D nitrogen-doped porous carbon with high capacitance. *Carbon* **2015**, *94*, 650–660.

[52] Yang, Y.; Lun, Z. Y.; Xia, G. L.; Zheng, F. C.; He, M. N.; Chen, Q. W. Non-precious alloy encapsulated in nitrogen-doped graphene layers derived from MOFs as an active and durable hydrogen evolution reaction catalyst. *Energy Environ. Sci.* **2015**, *8*, 3563–3571.

[53] Zhong, H. X.; Wang, J.; Zhang, Y. W.; Xu, W. L.; Xing, W.; Xu, D.; Zhang, Y. F.; Zhang, X. B. ZIF-8 derived graphene-based nitrogen-doped porous carbon sheets as highly efficient and durable oxygen reduction electrocatalysts. *Angew. Chem., Int. Ed.* **2014**, *53*, 14235–14239.

[54] Liu, Y. Y.; Zhang, W. N.; Li, S. Z.; Cui, C. L.; Wu, J.; Chen, H. Y.; Huo, F. W. Designable yolk–shell nanoparticle@MOF petalous heterostructures. *Chem. Mater.* **2014**, *26*, 1119–1125.

[55] Lü, Y. Y.; Zhan, W. W.; He, Y.; Wang, Y. T.; Kong, X. J.; Kuang, Q.; Xie, Z. X.; Zheng, L. S. MOF-templated synthesis of porous Co_3O_4 concave nanocubes with high specific surface area and their gas sensing properties. *ACS Appl. Mater. Interfaces* **2014**, *6*, 4186–4195.

[56] Torad, N. L.; Hu, M.; Ishihara, S.; Sukegawa, H.; Belik, A. A.; Imura, M.; Ariga, K.; Sakka, Y.; Yamauchi, Y. Direct synthesis of MOF-derived nanoporous carbon with magnetic Co nanoparticles toward efficient water treatment. *Small* **2014**, *10*, 2096–2107.

[57] Lü, Y. Y.; Wang, Y. T.; Li, H. L.; Lin, Y.; Jiang, Z. Y.; Xie, Z. X.; Kuang, Q.; Zheng, L. S. MOF-derived porous Co/C nanocomposites with excellent electromagnetic wave absorption properties. *ACS Appl. Mater. Interfaces* **2015**, *7*, 13604–13611.

[58] Metin, Ö.; Mazumder, V.; Özkar, S.; Sun, S. H. Monodisperse nickel nanoparticles and their catalysis in hydrolytic dehydrogenation of ammonia borane. *J. Am. Chem. Soc.* **2010**, *132*, 1468–1469.

[59] Seven, F.; Sahiner, N. Metal ion-imprinted hydrogel with magnetic properties and enhanced catalytic performances in hydrolysis of $NaBH_4$ and NH_3BH_3. *Int. J. Hydrogen Energy* **2013**, *38*, 15275–15284.

[60] Ye, W.; Zhang, H. M.; Xu, D. Y.; Ma, L.; Yi, B. L. Hydrogen generation utilizing alkaline sodium borohydride solution and supported cobalt catalyst. *J. Power Sources* **2007**, *164*, 544–548.

[61] Liu, B. H.; Li, Z. P.; Suda, S. Nickel- and cobalt-based catalysts for hydrogen generation by hydrolysis of borohydride. *J. Alloys Compd.* **2006**, *415*, 288–293.

[62] Feng, K.; Zhong, J.; Zhao, B. H.; Zhang, H.; Xu, L.; Sun, X. H.; Lee, S. T. $Cu_xCo_{1-x}O$ nanoparticles on graphene oxide as a synergistic catalyst for high-efficiency hydrolysis of ammonia-borane. *Angew. Chem., Int. Ed.* **2016**, *55*, 11950–11954.

[63] Akdim, O.; Demirci, U. B.; Miele, P. Deactivation and reactivation of cobalt in hydrolysis of sodium borohydride. *Int. J. Hydrogen Energy* **2011**, *36*, 13669–13675.

[64] Demirci, U. B.; Miele, P. Cobalt-based catalysts for the hydrolysis of $NaBH_4$ and NH_3BH_3. *Phys. Chem. Chem. Phys.* **2014**, *16*, 6872–6885.

[65] Ozerova, A. M.; Simagina, V. I.; Komova, O. V.; Netskina, O. V.; Odegova, G. V.; Bulavchenko, O. A.; Rudina, N. A. Cobalt borate catalysts for hydrogen production via hydrolysis of sodium borohydride. *J. Alloys Compd.* **2012**, *513*, 266–272.